Climatology of physical hydrographic and biological characteristics of the Northern South China Sea Shelf-sea (NoSoCS) and adjacent waters: Observations from satellite remote sensing

Xiaoju Pan [a,*], George T.F. Wong [a,b,**], Jen-Hua Tai [a], Tung-Yuan Ho [a]

[a] Research Center for Environmental Changes, Academia Sinica, Taipei, Taiwan
[b] Institute of Hydrological and Oceanic Sciences, National Central University, Jhongli, Taiwan

ARTICLE INFO

ABSTRACT

The climatology of the physical hydrographic and biological characteristics of the Northern South China Sea Shelf-sea (NoSoCS) are examined by using remotely sensed surface wind vectors, sea-surface temperatures (SST), surface chlorophyll-a concentrations (Chl_a), and vertically integrated net primary production (PP_{eu}), which can be generally validated by field observations. The annual average Chl_a and PP_{eu} in the NoSoCS are 1.1 ± 0.1 mg m^{-3} and 1.13 ± 0.07 g-C m^{-2} d^{-1}, respectively. The values of Chl_a and PP_{eu} in the inner shelf are about 7 and 3 times those in the outer shelf, respectively. Seasonally, in monthly averages, there are two distinct maxima, one in December/January and the other in July, at the height of the two monsoonal seasons, and two minima, in April/May and September during the two inter-monsoonal seasons, in both Chl_a and PP_{eu}. The maxima in Chl_a are of comparable magnitude. However, the winter maximum in PP_{eu} is about 30% larger than the summer maximum. These seasonal patterns are unique and are distinctly different not only from those generally found in the polar, temperate and tropical waters but also from those reported in the adjoining open South China Sea (SCS) where a summer maximum is absent. In the open SCS, monthly average Chl_a is negatively correlated to monthly average SST and positively correlated to monthly average wind speed. These correlations are consistent with the elevation of primary production in the winter as a result of the enhancement of vertical mixing by the combination of surface cooling and the stronger wind as hypothesized previously. In contrast, in the NoSoCS, monthly average Chl_a is not significantly correlated to monthly average SST and is only weakly correlated to monthly average wind speed, suggesting that other controlling processes may have come into play. These processes may include: (a) the terrestrial input of nutrients, especially through the discharge from the Pearl River, which reaches a maximum in the summer; (b) summer coastal upwelling off the Hainan Island and Dongshan and year-round upwelling off the Taiwan Bank; and (c) the enhanced vertical mixing by the action of internal waves along the outer shelf-upper slope. The influence of the discharge from the Pearl River is indicated by a tongue of water with elevated Chl_a that extends from the Pearl River mouth northeastward into the middle shelf in the summer. This water is also characterized by a positive correlation between monthly average Chl_a and SST together with no correlation or a slightly negative correlation between monthly average Chl_a and wind speed in individual pixels. Upwelling off the Taiwan Bank and the Hainan Bank are clearly depicted by an elevated Chl_a in the former and a depressed SST in the latter during the summer months. The temporal variations in the areal coverage of the upwelling water in the former are small, while the coverage in the latter reaches a maximum in July. The effect of the action of internal waves may be detected as a depression in SST and an elevation in Chl_a along the outer shelf-upper slope. The signals are especially noticeable at the Dongsha Plateau.

© 2015 Elsevier Ltd. All rights reserved.

* Corresponding author. Tel.: +886 2 26539885x861; fax: +886 2 27833584.
** Corresponding author at: Research Center for Environmental Changes, Academia Sinica, Taipei, Taiwan. Tel.: +886 2 26539885x861; fax: +886 2 27833584.
E-mail addresses: xpan@gate.sinica.edu.tw, xpanx001@gmail.com (X. Pan), gtfwong@gate.sinica.edu.tw (G.T.F. Wong).

1. Introduction

Shelf-seas constitute an important geochemical province of the world's oceans. Understanding their behaviors has not only regional but also global implications. For instance, while the shelf-seas account

for only about 7% of the area and less than 1% of the volume of the global oceans, they contribute about 22% of the primary production and 68% of fish catch in the global oceans (Pauly and Christensen, 1995). It would be difficult to have a firm grasp on the global marine primary production without an accurate handle on the contribution from the shelf-seas. A distinctive characteristic of the shelf-seas in comparison to the open oceans is that its biogeochemistry tends to be more temporally and spatially variable and the controlling processes are more diverse (Mann and Lazier, 1996). The influences of sub-regional processes, such as riverine discharge, coastal upwelling and the activities of internal waves, can be just as important, if not more important, as those of the basin-wide processes on distributional patterns (Mann and Lazier, 1996). In order to account for the highly dynamic effects of these sub-regional processes, establishing the mean state of the shelf-seas would require long term and frequent observations covering broad areas in the region. Obtaining this type of data would be a tall order through direct observations onboard ships. However, this is exactly the type of data that remote sensing can provide (Holman and Haller, 2013; McClain, 2009).

Recent studies have shown that the behaviors of the shelf-seas are not uniform as the primary environmental driving forces of their biogeochemistry can vary widely (Cai, 2011; Chen, 2003; Dai et al., 2013; Hofmann et al., 2011; Laruelle et al., 2010; Mann and Lazier, 1996). Among the different sub-sets of shelf-seas, the tropical shelf-seas constitute a significant sub-set but they have attracted relatively limited attention relative to their temperate counterpart (Cai, 2011; Laruelle et al., 2010; Mann and Lazier, 1996; Nittrouer et al., 1995; Wong et al., 2015). The South China Sea (SCS) is the largest tropical marginal sea of the world and the Northern South China Sea Shelf-sea (NoSoCS), which is situated at the northwestern corner of the SCS (Fig. 1), is among the largest sub-tropical shelf-seas in the world. Although the open SCS has been studied increasingly more intensively in the past several decades (Wong et al., 2007a) and it was the focus of several national and even international studies, such as the Tropical Ocean/Global Atmosphere (TOGA), Asian Seas International Acoustics Experiment (ASIAEX), South China Sea Monsoon Experiment (SCSMEX), Nonlinear Internal Waves Initiative/South China Sea Ocean Prediction Experiment (NLIWI/SCOPE) (Ramp and Tang, 2011) and the SouthEast Asian Time-series Study (SEATS) (Wong et al., 2007a), the shelf-seas around its rim have received much less attention. Previous studies on the NoSoCS tended to focus on sub-regional phenomena such as the characteristics of the Pearl River estuary (Callahan et al., 2004; Chen and Chen, 2006; Dai et al., 2008; Guo et al., 2008; Yin, 2002), the influence of the outflow from the Pearl River along the coast (Gan et al., 2009a, 2009b, 2010; Han et al., 2012; Song et al., 2012), upwelling off the Taiwan Bank (Wong et al., 2011), and the internal waves along the outer shelf and continental slope (Ramp and Tang, 2011). Synoptic studies on the NoSoCS as a whole are rare. In this study, the synoptic climatology of the physical hydrographic and biological characteristics of the NoSoCS and adjacent waters is constructed by using the remotely sensed data from multiple satellite sensors after they have been validated against field observations onboard ships.

2. Data and methods

2.1. The study area

The NoSoCS is situated in the subtropics and it forms part of the northwestern boundary of the SCS (Fig. 1). It stretches in a northeast-southwest direction from 23°N at the southern end of the Taiwan Strait to 20°N at the eastern coast of the Hainan Island and the Leizhou Peninsula for a distance of about 750 km, and from the coasts of southern China to the shelf edge at the 120-m isobaths for a distance of about 200 km. It covers an area of about 1.6×10^5 km². Although the NoSoCS is connected to the East China Sea through the Taiwan Strait at its northeastern boundary and to the Beibu Gulf through the Qiongzhou Strait at its southwestern boundary, exchange of water was restricted in the former case by a submarine ridge, with water depths of < 40 m, that extends from Dongshan seaward to the shelf edge, and in the latter case by the narrow Qiongzhou Strait, whose width is only about 30 km. Free exchange of water can only take place at its southeastern boundary between it and the open SCS. The Pearl River (Zhujiang), with one of the larger annual discharges (326 km³ yr^{-1}) among the rivers of the world, accounts for most of the terrestrial inputs to the NoSoCS and it reaches its peak flow in the summer (Dai et al., 2014; Guo et al., 2008; Wong et al., 2007a).

The NoSoCS may be subdivided into three primary hydrographic sub-regimes: the inner, middle and outer shelf with water depths of < 40 m, 40–90 m and 90–120 m, respectively (Wong et al., 2015). The hydrographic characteristics in the inner shelf are heavily influenced by the input of terrestrial material which results in lower salinity and higher concentrations in nutrients, dissolved organic matter, suspended particles and phytoplankton biomass (Callahan et al., 2004; Pan and Wong, 2015; Yin, 2002). The dominant phytoplankton group in these waters is generally the diatoms year round (Pan et al., 2013). On the other hand, the hydrographic characteristics in the outer shelf are governed primarily by mixing with the open oligotrophic SCS so that higher salinity and temperature and lower concentrations in nutrients, dissolved organic matter, suspended particles and phytoplankton biomass are generally found (Callahan et al., 2004; Pan and Wong, 2015; Tseng et al., 2005; Wong et al., 2007b). The dominant phytoplankton group in the outer shelf is generally *Prochlorococcus* in the summer and *Synechococcus* or haptophytes in the winter (Pan et al., 2013). The middle shelf water is a mixture of the inner shelf and outer shelf water. Superimposed on these shelf-wide patterns are secondary features that result from sub-regional processes, such as coastal upwelling (Gan et al., 2009b; Hong et al., 2009; Jing et al., 2009; Su and Pohlmann, 2009; Tang et al., 2002) and the activities of internal waves (Guo et al., 2012; Pan et al., 2012).

2.2. Field observations

Stations were occupied across the NoSoCS and in the adjacent waters in the northern SCS between 2008 and 2012 (Fig. 1 and Table 1). In addition, the SouthEast Asian Time-series Study
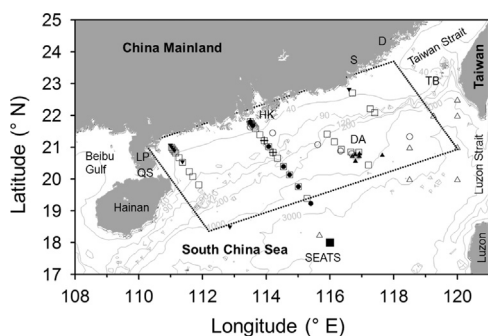
Fig. 1. The northern South China Sea Shelf-sea (NoSoCS) and station locations. Only the stations where there are match up satellite-derived and observed data in sea surface temperature (SST) or chlorophyll a concentration (Chl_a) are shown. Δ – Cruise OR1-866; ○ – Cruise OR3-1379; □ – Cruise OR1-929; ▾ – Cruise OR1-953; + – Cruise OR1-988; ● – Cruise OR1-1010; ▲ – Cruise OR1-1015; ■ – SouthEast Asian Time-series Study (SEATS) station. LP – Leizhou Peninsula; QS – Qiongzhou Strait; HK – Hong Kong; D – Dongshan; S – Shantou; DA – Dongsha Atoll; TB – Taiwan Bank; dotted lines enclosed area – area in which the hydrographic statistics in Table 2 were estimated.

Table 1
Field sampling cruises conducted and the data used in this study.

Cruises/Sources	Sampling periods	Data used	Number of stations[a]
(a) Data from cruises			
OR1-866	28 May–6 Jun 2008	CTD, Chl_a	6 (8)
OR3-1379	10–14 Jun 2009	CTD, Chl_a	6 (3)
OR1-929	3–12 Jun 2010	CTD, Chl_a	29 (6)
OR1-953	30 Dec 2010–6 Jan 2011	CTD, Chl_a	6 (2)
OR1-988	21–26 Dec 2011	CTD, Chl_a	3 (1)
OR1-1010	31 Aug–3 Sep 2012	CTD, Chl_a	5 (6)
OR1-1015	13–18 Oct 2012	CTD, Chl_a	7 (5)
SEATS	4 Sep 2002; 8–9 Nov 2004; 22 Jan 2005; 30 Mar 2005; 30 Jul 2005; 13–15 Oct 2010; 31 Aug–1 Sep 2012	CTD, Chl_a	7 (6)
(b) Data extracted from published literatures			
Chen et al. (2004)	1–12 Mar 2000	PP$_{eu}$	6
Chen (2005)	20–31 Mar 2001	PP$_{eu}$	6
	7–15 Mar 2002	PP$_{eu}$	6
	17–31 Oct 2002	PP$_{eu}$	8
	Jul 2000, Oct 2001, Jan 2003	PP$_{eu}$	3

[a] In (a), only the numbers of stations which match with the satellite observations of sea surface temperature and chlorophyll a concentration (in parenthesis) are shown.

(SEATS) station ($\sim$116°E, 18°N) was occupied seven times between 2002 and 2012 (Table 1). Each time when a station was occupied, the distributions of water temperature and salinity were recorded with depth with a conductivity-temperature-depth (CTD) recorder (SeaBird SBE9/11). Discrete water samples were collected by using 20-L Go-Flo bottles mounted onto a Rosette sampling assembly (General Oceanic) for the determination of the concentration of chlorophyll a (Chl_a), by fluorimetry (Strickland and Parsons, 1972) prior to 2007 and by high-performance liquid chromatography (HPLC) (Ho et al., 2015) in subsequent years.

In addition, primary production data reported in the published literatures were extracted from Chen et al. (2004) and Chen (2005) whose results were obtained between 2000 and 2003 (Table 1). Monthly average air temperature records at the Hong Kong Cheung Chau station (114.027°E, 22.201°N) between 2000 and 2012 were extracted from the Hong Kong Observatory (http://www.weather.gov.hk/cis/data/awsext_e.htm).

2.3. Remotely sensed data

Monthly Level-3 products of Chl_a and nighttime 4 μm sea surface temperature (SST) obtained with the MODerate resolution Imaging Spectroradiometer on Aqua sensor (MODIS-Aqua; Reprocessing R2013.1) between 2002 and 2012 with a spatial resolution of 9×9 and 4×4 km^2 respectively, and monthly Level-3 product of Chl_a obtained with the Sea-viewing Wide Field-of-view Sensor (SeaWiFS; Reprocessing R2010.0) between 1997 and 2007 with a spatial resolution of 9×9 km^2, in the area between 17° and 25°N and 110° and 121°E, were extracted from the NASA Ocean Color Web (http://oceancolor.gsfc.nasa.gov/). The corresponding monthly vertically integrated net primary production (PP$_{eu}$), which was estimated with a spatial resolution of 9×9 km^2 from the MODIS-Aqua (Reprocessing R2013.1) and SeaWiFS data (Reprocessing R2010.0) by using a Vertically Generalized Production Model (Behrenfeld and Falkowski, 1997), was extracted from the Ocean Productivity site (http://www.science.oregonstate.edu/ocean.productivity/index.php). Thus, the Chl_a and PP$_{eu}$ data used in this study in the time periods of 1997–2002, 2003–2007, and 2008–2012 were derived from the observations of the SeaWiFS sensor alone, both the SeaWiFS and MODIS-Aqua sensors, and the MODIS-Aqua sensor alone, respectively.

Chl_a data derived from the MODIS-Aqua and the SeaWiFS sensors in the global oceans have been shown to be consistent with each other (Maritorena et al., 2010; Morel et al., 2007). In a more regional study in the northern SCS, Zhang et al. (2006) reported that they also agreed reasonably well with field observations. Thus, the Chl_a data from these two sources were merged and used interchangeable in this study so as to cover the entire time span between 1997 and 2012. However, it is well known that the satellite-derived Chl_a and PP$_{eu}$ by using the global algorithms are less reliable in Case-2 waters (Pan et al., 2008, 2010), such as those in the inner shelf in the NoSoCS, as a result of the contributions from the elevated concentrations of suspended sediments and colored dissolved organic matter (CDOM) (Gordon and Morel, 1983). In the SCS, including the NoSoCS, Tang et al. (2008) reported that Chl_a is typically overestimated year round when the global algorithm is applied to the remotely sensed data, probably as a result of the presence of the relatively high concentrations of CDOM. Pan et al. (2008) reported similar findings in the south Middle Atlantic Bight, another shelf-sea. Nevertheless, since the extent of the overestimations may be assessed by comparing the satellite-derived and the observed values, the overestimation is independent of the time of the year, and the concentration differences among the waters in the NoSoCS exceed these overestimations significantly, the spatial and temporal patterns are still valid qualitatively.

Daily MODIS-Aqua Level-2 products (Reprocessing R2013.1), including SST and Chl_a, with the native spatial resolution (about 1×1 km^2) in the area between 17° and 25°N and 110° and 121°E between 2002 and 2012 were also downloaded from the NASA Ocean Color Web. They were used for satellite validation. For the validation on PP$_{eu}$, the 8-day binned values with a spatial resolution of 9×9 km^2, also extracted from the Ocean Productivity site, were used.

Monthly surface (10 m above the sea surface) wind vector data (version v4), with a spatial resolution of about 25×25 km^2, obtained by the QSCAT sensor between July 1999 and November 2009 were extracted from the Remote Sensing System (http://www.ssmi.com/).

3. Results and discussions

3.1. Validation of the satellite derived products

The satellite-derived data in SST, Chl_a and PP$_{eu}$ were validated by comparing them to field observations, following the protocols of Bailey and Werdell (2006). A more detailed description of this procedure can be found in Pan et al. (2008, 2010, 2013). For SST and Chl_a, the remotely sensed value in a 3×3 pixel array (or approximate 3×3 km^2) centered on each of the field stations was compared to the observed value. The pixels were masked by the flags described in Bailey and Werdell (2006). A satellite overpass time-window of ± 72 h from the field observations was used. For PP$_{eu}$, the binned 8-day average value in an area of approximate 9×9 km^2

centered on each of the field station was compared to the observed value. The equivalent satellite overpass time-window was about ± 96 h from the field observations. Ideally, a narrower time-window, ± 3 h, is preferred (Bailey and Werdell, 2006). A wider time-window was used here because of the paucity of remotely sensed data in the study area as a result of the frequent cloud cover. At a time-window of ± 3 h, there was almost no match-up data between the satellite observations and the field measurements. Some of the sub-regions in the NoSoCS, such as the areas with intense activities of the internal waves north of the Dongsha Atoll and east of the Hainan Island, are known to be physically highly dynamic, and thus significant short-term variations in SST and Chl_a can be expected (Guo et al., 2012; Li et al., 2008; Pan et al., 2012; Shaw et al., 2009). In view of the wider time-window used, the data from these sub-regions were excluded from this comparison. Even then, the wider time-window used likely has introduced additional uncertainty into the comparison as a result of the temporal variability (Pan et al., 2008, 2010). Thus, this comparison likely represents a worst case scenario.

The root mean square error (RMSE) was used to evaluate the goodness-of-fit between the field observations and the corresponding values derived from remote sensing such that:

$$\text{RMSE} = \sqrt{\sum (P_d - P_f)^2 / n} \qquad (1)$$

Here, n is the number of match-up samples, the subscripts d and f denote values derived by remote sensing and found in field measurements respectively, and P may be SST, $\log(\text{Chl}\_a)$ or $\log(\text{PP}_{eu})$. The logarithmic scale was used in the latter two cases in order to accommodate their wide range of values, which varied by over an order of magnitude.

The RMSEs in SST, $\log(\text{Chl}\_a)$ and $\log(\text{PP}_{eu})$ were $0.59\ ^\circ\text{C}$ ($n=69$), 0.222 ($n=37$) and 0.20 ($n=38$), respectively (Fig. 2). The latter two can be converted to a range in the ratios of $(\text{Chl}\_a)_d$ to $(\text{Chl}\_a)_f$ of 0.6 to 1.7, and of $(\text{PP}_{eu})_d$ to $(\text{PP}_{eu})_f$ of 0.6 to 1.6 (Fig. 2B, C). These RMSEs are within the ranges found in other attempts to validate this type of remotely sensed data (Behrenfeld and Falkowski, 1997; O'Reilly et al., 1998; Pan et al., 2008, 2010; Zhang et al., 2006). Only the Chl_a data derived from MODIS-Aqua were used in the comparison as no field observation was made while the SeaWiFS sensor was in operation. Nevertheless, since previous work has indicated that the errors in Chl_a derived from SeaWiFS and MODIS-Aqua are comparable to each other (Zhang et al., 2006), the uncertainty in Chl_a derived from SeaWiFS in this study was assumed to be similar to that from MODIS-Aqua. In the case of PP_{eu}, only data from outside of the inner shelf was available for the comparison and the RSME stayed about the same when the data set was sub-divided into those derived from each of the two satellite sensors. Since PP_{eu} was estimated from the combination of the derived Chl_a and SST and its RSME was almost identical to that of Chl_a alone, SST was probably only a minor contributor to its total error.

The relationships between the remotely sensed values and the corresponding field observations (Fig. 2) can be given by a Model II regression analysis as:

$$\text{SST}_d = (0.75 \pm 0.47) + (0.96 \pm 0.02)\ \text{SST}_f;$$
$$r^2 = 0.976,\ n = 69,\ P < 0.001 \qquad (2)$$

$$\log(\text{Chl}\_a)_d = (0.03 \pm 0.09) + (1.22 \pm 0.12)\log(\text{Chl}\_a)_f$$
$$r^2 = 0.750,\ n = 37,\ P < 0.001 \qquad (3)$$

$$\log(\text{PP}_{eu})_d = (-0.06 \pm 0.08) + (0.78 \pm 0.17)\log(\text{PP}_{eu})_f$$
$$r^2 = 0.347,\ n = 38,\ P < 0.001 \qquad (4)$$

In all cases, taking into account the statistical uncertainties, the intercepts were close to zero and the slopes were close to unity, suggesting that the derived values represented the observed values
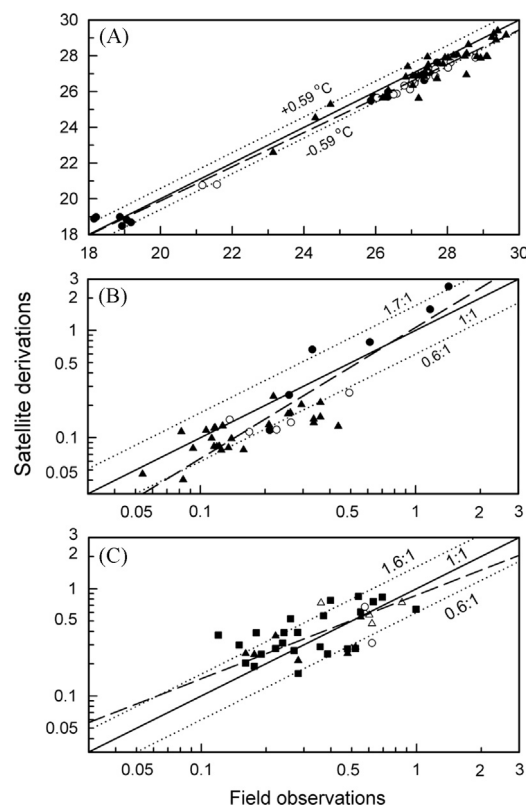
Fig. 2. The relationships between field observations and (A) MODIS-Aqua derived SST ($^\circ$C), (B) log-transformed MODIS-Aqua derived Chl_a (mg m^{-3}) and (C) log-transformed SeaWiFS and MODIS-Aqua derived PP$_{eu}$ (g-C m^{-2} d^{-1}). Solid lines – 1:1 relationships; dotted lines – the root mean square errors of the estimated values from the 1:1 lines; dashed lines – Model II linear regressions according to Eqs. (2)–(4). $\bullet$, $\circ$, $\blacktriangle$ – by MODIS-Aqua in the inner shelf, middle shelf, and outer shelf/open SCS; $\triangle$, $\blacksquare$ – by SeaWiFS in the middle shelf and outer shelf/open SCS.

well and, if there was a systematic error, it was small. Few data points fell outside of ± 1 RMSE so that the satellite-derived data may be interpreted to within these ranges. Nevertheless, upon closer examination, there was an indication that the derived values in Chl_a tended to be higher, by up to 70%, than the observed values at the higher concentrations above 0.4 mg m^{-3} in the inner shelf (Fig. 2B). These larger discrepancies in the inner shelf are an indication of the widely recognized limitation in the application of the global algorithms for estimating Chl_a from remotely sensed data to the Case-2 coastal waters (Pan et al., 2008, 2010; Tang et al., 2008; Zhang et al., 2006). Furthermore, the correlation coefficient in $\log(\text{PP}_{eu})$ was noticeably lower than those in SST and $\log(\text{Chl}\_a)$, indicating that the estimation of PP_{eu} from remotely sensed data was less reliable. This was not unexpected as the remotely sensed PP_{eu} was estimated from Chl_a and SST based on a biological–physical model (Behrenfeld and Falkowski, 1997) so that its uncertainty included the sum of the uncertainties in both Chl_a and SST plus those in the model assumptions. Furthermore, in this study, the potential mismatch between the satellite-derived and observed values in PP_{eu} was also inherently larger than that in Chl_a as the satellite derived PP_{eu} was an average over a substantially larger area obtained within a wider satellite overpass time-window.

3.2. Distributions of monthly average surface wind, SST and Chl_a

The distributions of monthly average surface wind in 1999–2009 and SST and Chl_a in 2002–2012 in the NoSoCS and the adjacent northern SCS are shown in Figs. 3–5. As reported previously (Gan et al., 2006; Shaw and Chao, 1994), steady and strong northeast wind, frequently exceeding 10 m s^{-1}, covers the entire northern SCS from
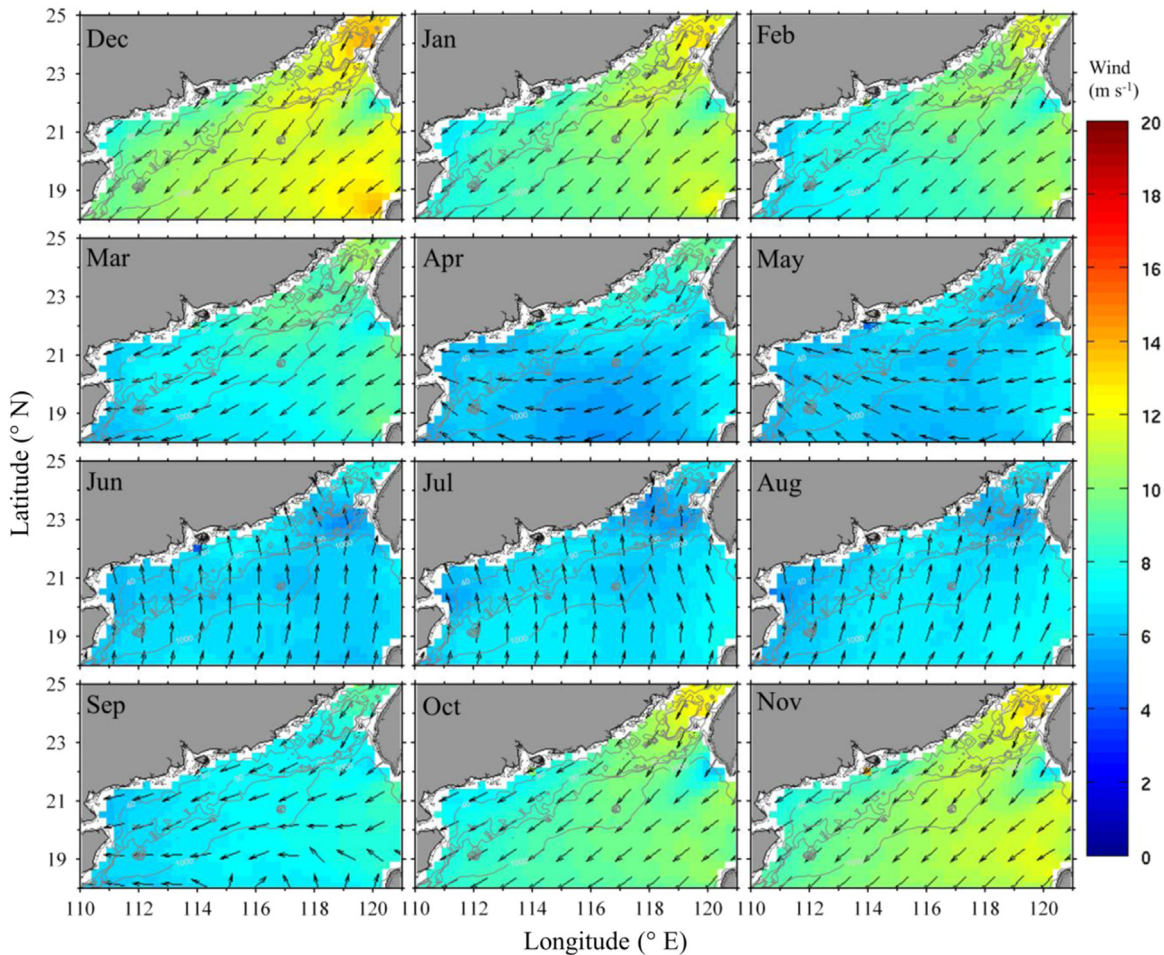
Fig. 3. The distributions of QSCAT-derived average monthly surface wind speed and direction in 1999–2009.

October through March, while weaker, usually less than 8 m s^{-1}, south wind is found between June and August (Fig. 3). The wind direction is latitudinally more variable during the inter-monsoonal seasons, as it changes progressively from the northeast at the higher latitudes to the east and then the southeast at the lower latitudes in April and May and again in September. Between these two inter-monsoonal seasons, the spring inter-monsoonal season is longer and better defined as its wind speed is lower and its wind direction is more easterly than those in both monsoonal seasons (Fig. 3). In most months, there is also generally a decrease in wind speed from the north to the south and from the east toward the coast in the west. As a result, the wind speed in the NoSoCS tends to be lower than that in the adjacent open SCS (Fig. 3).

There is a general trend of decreasing SST with increasing latitude and with decreasing distance from land in the NoSoCS (Fig. 4) as reported previously (Chu et al., 1997). They reflect the latitudinal dependence of the seasonal heat loss and heat gain across the air–sea interface and the year-round discharge of generally colder terrestrial water into the NoSoCS. Since the NoSoCS extends from the northeast to the southwest, these two trends lead to an along-shelf as well as a cross-shelf SST gradient of several degrees in Celsius. On the other hand, the distribution of Chl_a is dominated by a cross-shelf increase in concentration towards the coast (Fig. 5), as a result of the enhancement of biological activities along the coasts by the input of terrestrial nutrients (Mann and Lazier, 1996). Changes in Chl_a along the shelf are relatively small. The depression in SST, up to about 5 °C, and the elevation in Chl_a, up to about 2 mg m^{-3}, across the shelf are especially conspicuous between the middle shelf and the inner shelf.

Superimposed on these regional trends are several seasonal sub-regional features. The intrusion of water along the coast during the northeast monsoonal season from the Taiwan Strait into the NoSoCS (Hu et al., 2010) is indicated by the patch of water with significantly lower temperature, < 18 °C in December through March, at the northeastern corner of the Shelf-sea. This patch of water reaches its maximum areal coverage in January as the temperature dips to < 15 °C. The topographically induced upwelling at the seaward outer edge of the Taiwan Bank as a result of its interaction with the intruding Kuroshio (Hu et al., 2003, 2010) is captured as an isolated patch of water with depressed temperature, < 28 °C in June through September, and elevated Chl_a, > 1.2 mg m^{-3} in April through September. Though this upwelling may occur year-round (Hong et al., 2009, 2011; Hu et al., 2003, 2010; Shang et al., 2011; Shen et al., 2008; Tang et al., 2002, 2004), the signal can be unequivocally depicted by an elevation in Chl_a only in April through September when the upwelling water is clearly separated from the coastal water further landward, which is also characterized by colder temperatures and higher Chl_a. Summer coastal upwelling off Dongshan as a result of Ekman transport and topography (Gan et al., 2009a, 2009b; Hong et al., 2009, 2011; Hu et al., 2003, 2010; Tang et al., 2002, 2004; Wang et al., 2012) can also be detected as water with lower temperature (< 27 °C) and as a seaward expansion of the areal coverage of water with elevated Chl_a (> 1 mg m^{-3}) at around 23.5°N and 117.5°E in June through August. The patch of water with depressed temperature (< 28 °C in June through August) at the northeastern corner of the Hainan Island during the southwest monsoon is consistent with the effect of wind-induced upwelling
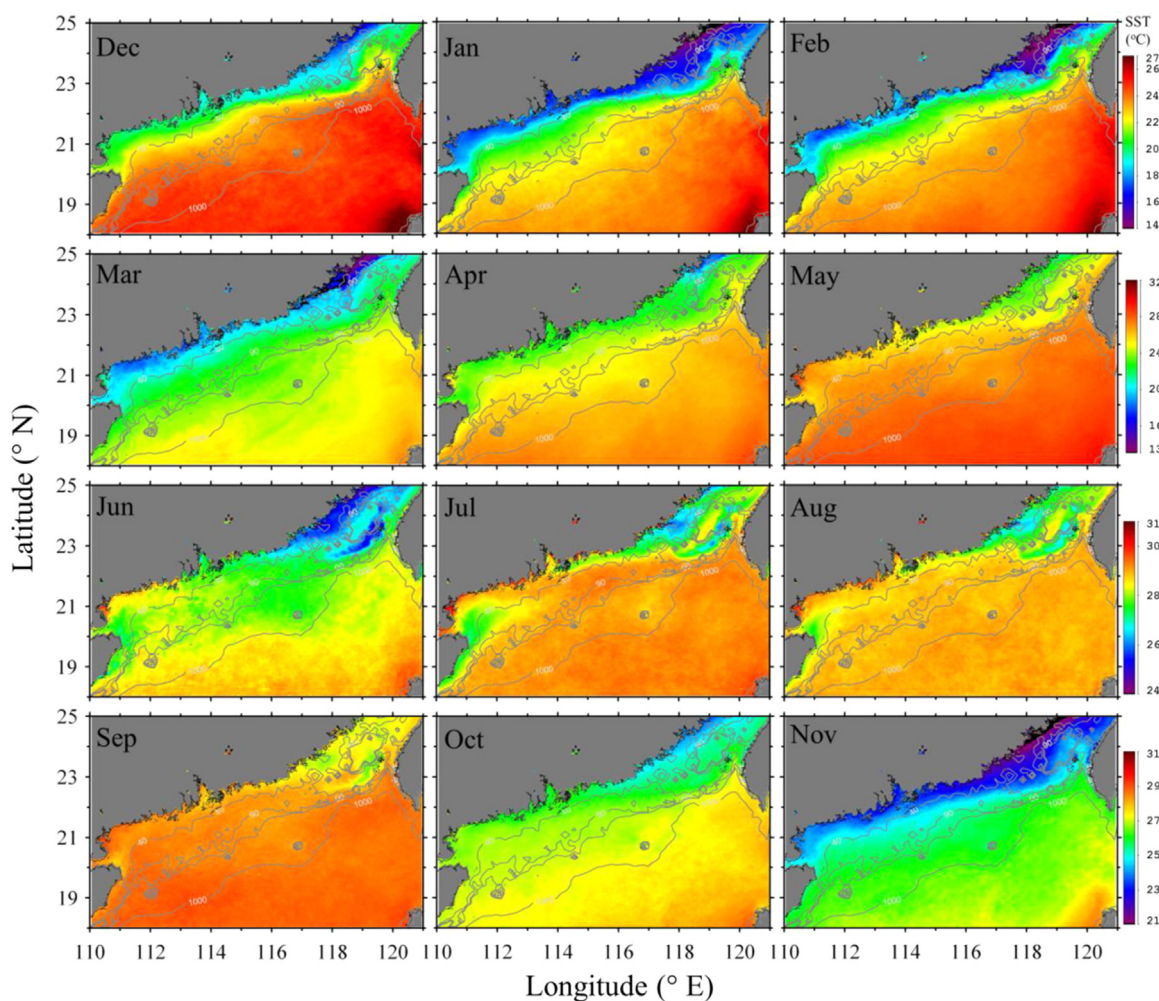
Fig. 4. The distributions of MODIS-Aqua-derived climatological monthly average SST in 2002–2012. Note that different color scale is used in each row of figures.

in the summer months (Jing et al., 2009; Song et al., 2012; Su and Pohlmann, 2009) and it reaches its maximum areal extent in July. A companion signal of elevated Chl_a cannot be clearly identified as the influence from the upwelling can be masked by mixing with the coastal waters with high Chl_a. On the other hand, while the influence of the outflow from the Pearl River on the NoSoCS cannot be clearly indicated in the regional distribution of SST, it can be detected readily in the distribution of Chl_a. During the winter months, the outflow from the Pearl River is at its minimum (Guo et al., 2008; Wong et al., 2007a) and the strip of water with elevated Chl_a along the coast is narrow and is confined to within the inner shelf. During the period of maximum outflow from the Pearl River, which occurs historically in June/July (Guo et al., 2008; Wong et al., 2007a), a tongue of water with elevated Chl_a (>1 mg m^{-3}) can be traced from the mouth of the Pearl River northeastward into the middle shelf.

3.3. Monthly average hydrographic characteristics

The climatological monthly average wind vector and scalar wind speed in 1999–2009, SST in 2002–2012, and Chl_a and PP$_{eu}$ in 1997–2012 in the NoSoCS as a whole and the adjacent open SCS are shown in Fig. 6, while those in the inner, middle and outer shelf of the NoSoCS are shown in Fig. 7. The climatological annual averages, as well as the averages during the northeast and south-west monsoonal seasons, are also listed in Table 2.

The annual average wind speed in the NoSoCS is about 7.8 m s^{-1} (Fig. 6A, B, Table 2). The minimum monthly average wind speed of 6.4 m s^{-1} is found in May during the spring inter-monsoonal months (Fig. 6A, B). In the ensuing southwest monsoonal season between June and August, the wind is steady and it stays weak, at about 6.5 m s^{-1} (Fig. 6A, B). During the fall inter-monsoonal seasonal in September, the wind speed does not deviate much from those during the southwest monsoon. Then, it increases steadily from October to a maximum of 10.3 m s^{-1} in December before it drops progressively back to the low value in May (Fig. 6A, B). While the wind directions in the NoSoCS and the adjacent open SCS are similar to each other (Fig. 3), the wind speed in the former tends to be lower in most months (Fig. 6B, Table 2). However, the difference is small, usually within 0.5 m s^{-1} and this drop in wind speed occurs primarily from the middle shelf to the inner shelf (Fig. 7A, Table 2). As an indication of the inter-annual variability, the standard deviations of the monthly average values in the inner, middle and outer shelf, at ± 0.3 to ± 1.2 m s^{-1} (Fig. 7A), are much larger than the variations among these three hydrographic sub-regimes but smaller than the seasonal variations, indicating that the effect of seasonal variations is larger than that of inter-annual variations which in turn is larger than that of the spatial variations in the NoSoCS (Fig. 7A).

The annual average SST in the NoSoCS is about 25 °C (Fig. 6C, Table 2). The pattern in the seasonal changes in SST follows that in air temperature closely (Fig. 7B), indicating effective heat exchange between air and sea. The lowest monthly average SST, 20 °C, is found in January while the maximum value, 29 °C, is found in July and August (Fig. 6C). The SST in NoSoCS is invariably lower than that in the open SCS but higher than the air temperature. The temperature difference is larger in the winter months than in the
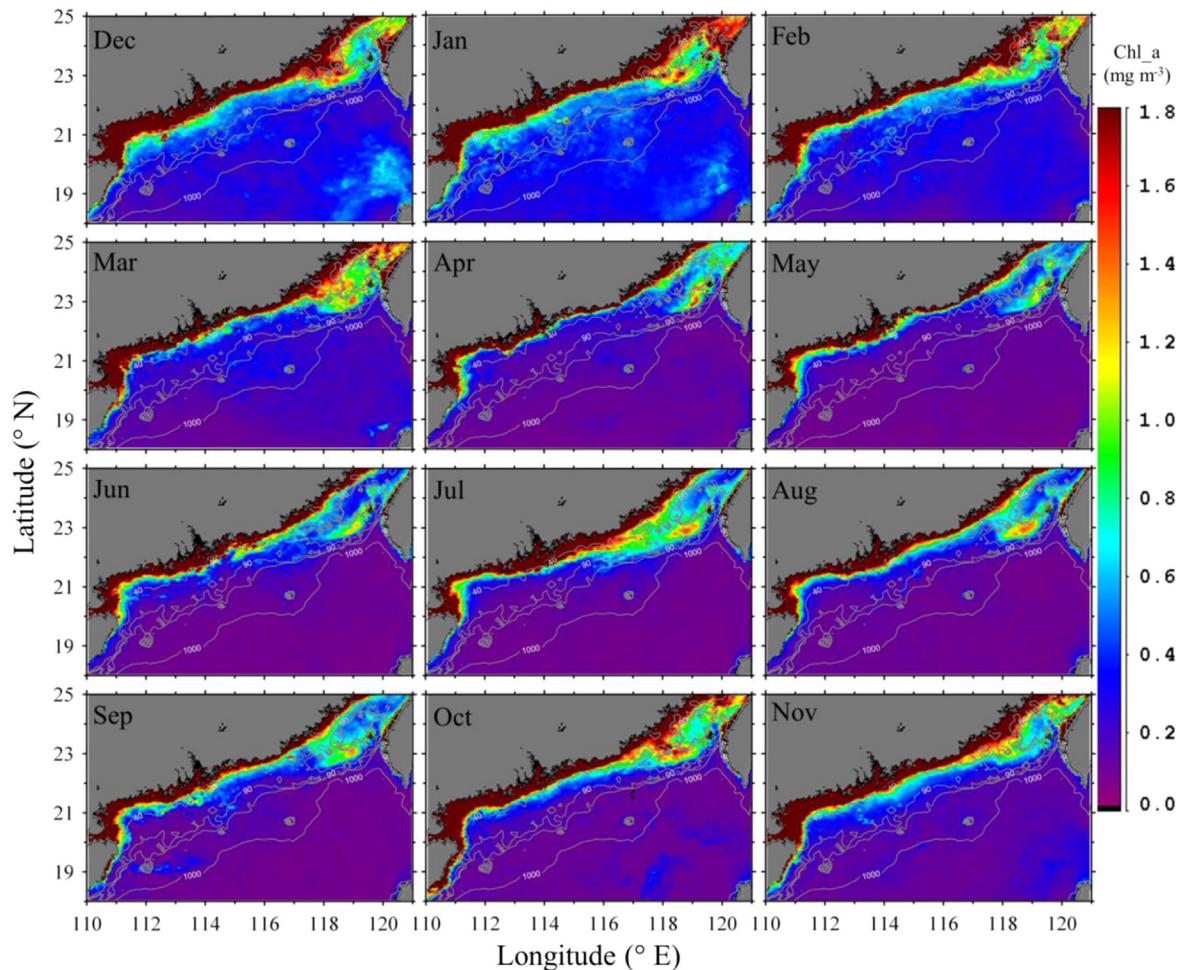
Fig. 5. The distributions of MODIS-Aqua-derived climatological monthly average Chl_a in 2002–2012.

summer months. Within the NoSoCS, SST decreases landward (Fig. 7B). The drop in temperature is larger between the inner and middle shelf than between the middle and outer shelf and during the winter months than during the summer months. Thus, the temperature difference between the inner and the outer shelf is $< 0.7\,°C$ in July and August but it reaches $3.5\,°C$ in December and January (Fig. 7B). The standard deviations in the monthly average SST, mostly about $0.6\,°C$, are relatively constant in all the months in the year and they are smaller than both the seasonal and the spatial variations (Table 2), indicating that the inter-annual variability in SST is smaller than the seasonal and spatial variations.

The NoSoCS is moderately productive. Its annual average Chl_a, $1.1\,\text{mg m}^{-3}$, is well within the range of values reported in shelf-seas (Szeto et al., 2011) but it is about 6 times that, $0.19\,\text{mg m}^{-3}$, in the open SCS (Table 2). The seasonal variations in Chl_a in the open SCS follows a distinct seasonal pattern (Fig. 6D) as previously reported (Liu et al., 2002, 2013; Shen et al., 2008; Tseng et al., 2005), with a summer minimum of about $0.13\,\text{mg m}^{-3}$ between June and August and a winter maximum of about $0.35\,\text{mg m}^{-3}$ in January (Fig. 6D). However, in the NoSoCS, in addition to the winter maximum, there is also a summer maximum in July when Chl_a, up to about $1.3\,\text{mg m}^{-3}$, can rival those found in December and January (Fig. 6D). This summer maximum in Chl_a is consistent with the enhancement of primary production by the input of nutrients from the Pearl River which reaches its peak flow at about the same time when the flow is almost one order of magnitude higher than that in the winter months (Guo et al., 2008; Wong et al., 2007a) and Chl_a

in the river water may reach $10\,\text{mg m}^{-3}$ (Yin, 2002). Accompanying the two maxima are two minima in Chl_a in April–May and in September during the inter-monsoonal seasons. Between these two minima, Chl_a is lower in April–May ($\sim 0.6\,\text{mg m}^{-3}$) than in September ($\sim 1.0\,\text{mg m}^{-3}$). This seasonal pattern is unique as it is different not only from that in the adjoining open SCS but also from the generally seasonal patterns in the polar, temperate and tropical waters (Yoder et al., 1993, 2002).

Across the NoSoCS, Chl_a increases landward as the concentration in the inner shelf is about one order of magnitude higher than that in the outer shelf and the open SCS (Fig. 7C, Table 2). The increase is more abrupt, $\sim 1.5\,\text{mg m}^{-3}$, from the middle to the inner shelf than, $\sim 0.24\,\text{mg m}^{-3}$, from the outer to the middle shelf. Furthermore, while the winter maximum is well developed in all the hydrographic sub-regimes, the summer maximum becomes increasingly more prominent towards the coast so that the concentration in the summer maximum becomes virtually the same as that in the winter maximum in the middle and inner shelf (Figs. 4, and 7C). This is consistent with the enhancement of the increasing influence of terrestrial material on biological productivity towards the coast. Among the hydrographic sub-regimes, the standard deviations in the monthly averages in Chl_a are the largest, around $0.4\,\text{mg m}^{-3}$, in the inner shelf and they are equivalent to about 23% of the monthly averages and 35% of the annual range (Fig. 7C). These indicate that inter-annual variations in Chl_a can be significant relative to the annual variations. Nonetheless, both of them are still smaller than the spatial variability as the concentration in the inner shelf can exceed that in the outer shelf by close to $2\,\text{mg m}^{-3}$ (Table 2). While
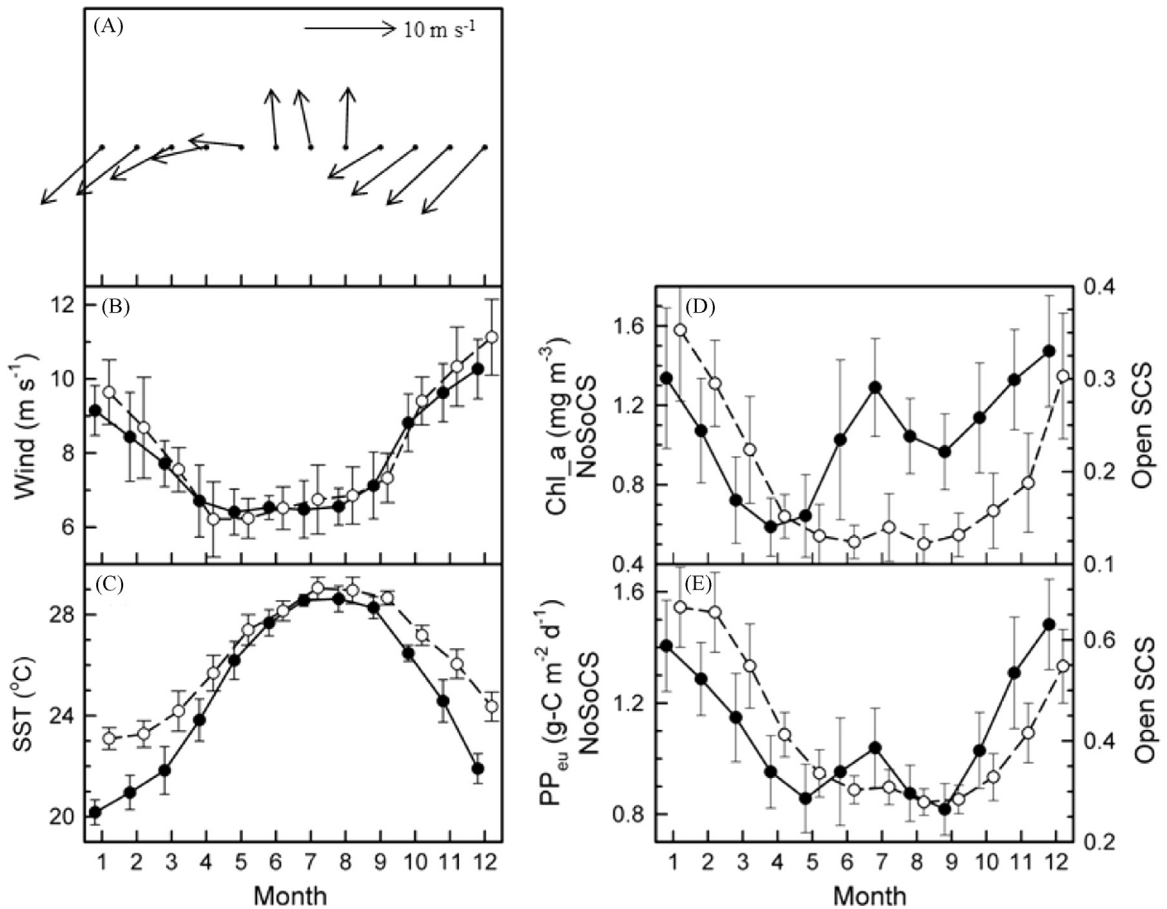
Fig. 6. The climatological monthly average (A) wind vector in 1999–2009 in the NoSoCS, and (B) scalar wind speed in 1999–2009, (C) SST in 2002–2012, (D) Chl_a and (E) PP$_{eu}$ in 1997–2012 in the NoSoCS (●) and the adjacent open SCS (○).The error bars represent one standard deviation from the average values.
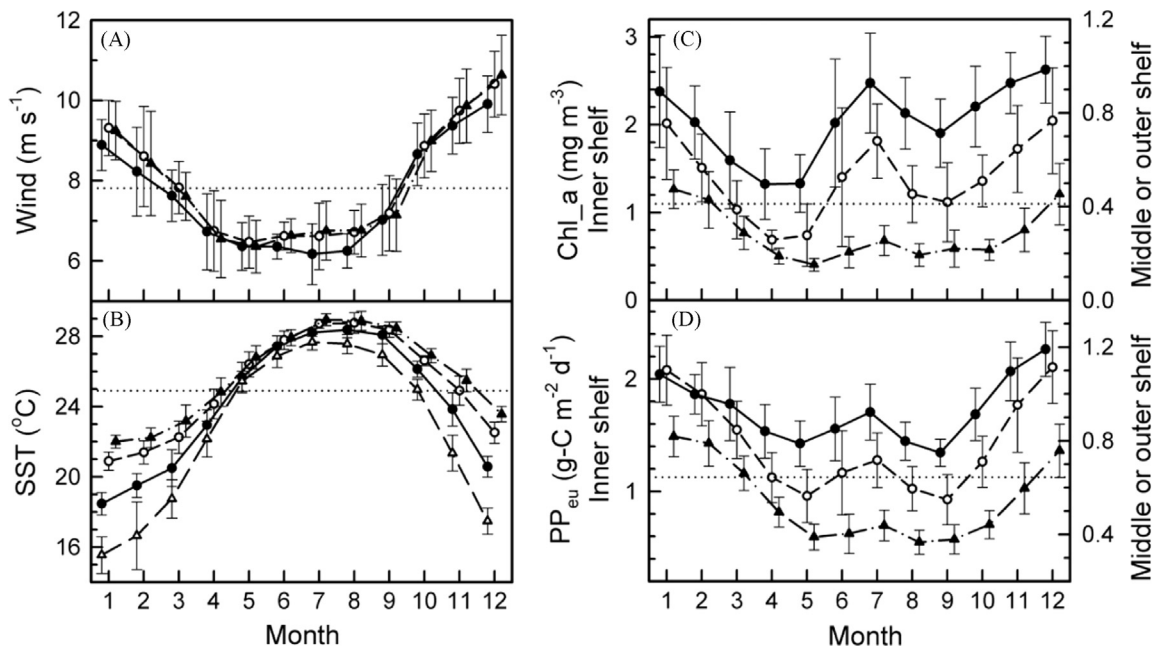
Fig. 7. The climatological monthly average (A) scalar wind speed in 1999–2009, (B) SST in 2002–2012, and (C) Chl_a and (D) PP$_{eu}$ in 1997–2012 in the inner (●), middle (○), and outer shelf (▲) of the NoSoCS. The annual means in the NoSoCS are shown by the dotted lines. △ – climatological monthly average air temperatures in 2000–2012 in (B). The error bars represent one standard deviation from the average values.

Chl_a might have been overestimated by applying the global algorithms to remotely sensed data at the higher concentrations in the inner shelf (Fig. 2B; Tang et al., 2008; Zhang et al., 2006) and this would have resulted in overestimations in the average concentration in the NoSoCS and the concentration ratio between the inner and outer shelf, these general spatial and temporal patterns in the

Table 2
Statistics (mean ± SD) of the climatology of the environmental conditions and biological activities in the NoSoCS and adjacent open South China Sea (SCS).

Parameters[a]	Seasons[b]	Northern South China Sea Shelf-sea (NoSoCS)				Open SCS
		Inner	Middle	Outer	Whole shelf	
Bathymetry (m)		≤ 40	40–90	90–120	≤ 120	> 120
Area (10^4 km^2)		6.50	6.78	2.83	16.11	14.3
Volume (10^{12} m^3)		1.12	4.22	2.73	8.07	129.1
Mean depth (m)		17.3	62.3	96.4	50.1	903.5
Scalar wind (m s^{-1})	SW	6.28 ± 0.24	6.65 ± 0.30	6.71 ± 0.32	6.52 ± 0.27	6.70 ± 0.37
	NE	8.49 ± 0.39	8.80 ± 0.47	8.78 ± 0.50	8.68 ± 0.44	9.00 ± 0.49
	Annual	7.64 ± 0.24	7.93 ± 0.31	7.91 ± 0.32	7.82 ± 0.28	8.04 ± 0.31
SST (°C)	SW	28.0 ± 0.3	28.4 ± 0.3	28.6 ± 0.3	28.3 ± 0.3	28.7 ± 0.3
	NE	21.7 ± 0.4	23.3 ± 0.4	24.0 ± 0.4	22.8 ± 0.4	24.8 ± 0.3
	Annual	24.1 ± 0.2	25.2 ± 0.2	25.8 ± 0.2	24.9 ± 0.2	26.3 ± 0.2
Chl_a (mg m^{-3})	SW	2.21 ± 0.35	0.55 ± 0.13	0.22 ± 0.04	1.16 ± 0.19	0.13 ± 0.02
	NE	2.10 ± 0.23	0.57 ± 0.12	0.34 ± 0.05	1.15 ± 0.15	0.24 ± 0.03
	Annual	2.05 ± 0.21	0.53 ± 0.07	0.28 ± 0.03	1.10 ± 0.12	0.19 ± 0.01
PP$_{eu}$ (g-C m^{-2} d^{-1})	SW	1.57 ± 0.18	0.66 ± 0.08	0.40 ± 0.05	0.98 ± 0.11	0.30 ± 0.02
	NE	1.89 ± 0.16	0.91 ± 0.10	0.65 ± 0.05	1.26 ± 0.11	0.51 ± 0.05
	Annual	1.73 ± 0.12	0.79 ± 0.05	0.55 ± 0.02	1.13 ± 0.07	0.43 ± 0.02

[a] SST – sea surface temperature; Chl_a – sea surface concentration of chlorophyll a; PP$_{eu}$ – vertically integrated primary production.
[b] SW: southwest monsoonal season (June–August); NE: northeast monsoonal season (October–April).

variations in Chl_a are not affected even when an overestimation of 70%, the upper limit indicated by the RSME in log(Chl_a), was allowed.

The annual average PP$_{eu}$ in the NoSoCS is estimated to be 1.1 g-C m^{-2} d^{-1} (Table 2), or 66 T g-C yr^{-1} (1 T g=10^{12}g) for the whole Shelf-sea. The spatial and seasonal distributional patterns in PP$_{eu}$ in the open SCS, the NoSoCS and the hydrographic sub-regimes within the NoSoCS (Figs. 6E, and 7D) are similar to those in Chl_a and they are consistent with those reported in field observations (Chen, 2005; Chen and Chen, 2006; Chen et al., 2004). Thus, while there is a single summer minimum and a single winter maximum in PP$_{eu}$ in the open SCS, in the NoSoCS and its hydrographic sub-regimes, there are two maxima, one in the winter and one in the summer, and two minima, one in the spring and one in the fall. Furthermore, PP$_{eu}$ increases and its summer maximum becomes more conspicuous shoreward and the increase in PP$_{eu}$ is more conspicuous from the middle to the inner shelf. On the other hand, unlike Chl_a, the summer maximum in PP$_{eu}$, about 1.0 g-C m^{-2} d^{-1} in July, is more subdue as it is only about 70% of that of the winter maximum in December. The minima in PP$_{eu}$, both at about 0.8 g-C m^{-2} d^{-1}, are of about the same magnitude in May and September.

3.4. Regional phenomenon – seasonal vertical convective mixing by wind and surface heating/cooling

The relationship between the monthly average Chl_a and SST, wind speed (W), and the combination of the two in the open SCS can be expressed in a Model II linear regression analysis as:

$$\text{Chl\_a} = (1.08 \pm 0.06) - (0.034 \pm 0.002)\,\text{SST}$$
$$r^2 = 0.679; \ n = 126; \ P < 0.001 \tag{5}$$

$$\text{Chl\_a} = (-0.05 \pm 0.03) + (0.031 \pm 0.004)W$$
$$r^2 = 0.378; \ n = 125; \ P < 0.001 \tag{6}$$

$$\text{Chl\_a} = (-0.60 \pm 0.29) + (0.027 \pm 0.011)\,\text{SST} + (0.20 \pm 0.04)\,W$$
$$- (0.007 \pm 0.001)\,\text{SST} \times W$$
$$r^2 = 0.811; \ n = 89; \ P < 0.001 \tag{7}$$

Thus, Chl_a is negatively correlated with SST and positively correlated with wind speed. Furthermore, while Chl_a is significantly correlated with SST and wind speed individually, the correlation is much stronger when both are involved. These relationships are consistent with the control of the seasonal pattern in Chl_a in the

open northern SCS by the elevation in primary production in the winter as a result of the increasing availability of the nutrients from the subsurface water by the enhanced vertical mixing caused by the combination of surface cooling and the higher wind speed (Tseng et al., 2005). Individually, neither one of these processes is sufficient for providing the necessary vertical mixing to account for the elevation in Chl_a. Spatially, the correlation coefficients, r, between Chl_a and SST and between Chl_a and wind speed in each pixel range from −0.6 to −0.8 (Fig. 8A) and from 0.4 to 0.6 (Fig. 8B) respectively in almost the entire open SCS. While SST is also moderately negatively correlated with wind speed in the open SCS (Fig. 8C) with correlation coefficients of −0.5 to −0.8, this statistical coincidence cannot totally account for the correlation of Chl_a to the both of them. The seasonal variations in SST and wind speed are not exactly in phase and their respective minima and maxima do not coincide exactly (Figs. 6 and 7). The pattern in the spatial distribution of the correlation coefficients between SST and wind speed (Fig. 8C) do not correspond to those between Chl_a and SST (Fig. 8A) and between Chl_a and wind speed (Fig. 8B) exactly. For example, while there is an abrupt drop in the correlation coefficient between SST and wind at about 118°E so that the values are invariably more negative than −0.6 east of 118°E and stay rather uniform at about −0.55 west of 118°E, the distribution is more variable and sporadic in the relationship between Chl_a and wind speed but more uniform in the relationship between Chl_a and SST. These mismatches indicate that the correlation between Chl_a and SST and wind speed is not just a statistical coincidence.

The corresponding relationships between the monthly average Chl_a and SST, wind speed (W), and the combination of the two in the NoSoCS are:

$$\text{Chl\_a} = (1.58 \pm 0.29) - (0.020 \pm 0.012)\,\text{SST}$$
$$r^2 = 0.017; \ n = 126; \ P = 0.151 \tag{8}$$

$$\text{Chl\_a} = (0.20 \pm 0.15) + (0.11 \pm 0.02)\,W$$
$$r^2 = 0.235, \ n = 125, \ P < 0.001 \tag{9}$$

$$\text{Chl\_a} = (-7.6 \pm 1.6) + (0.30 \pm 0.06)\,\text{SST} + (0.99 \pm 0.20)W$$
$$- (0.034 \pm 0.008)\,\text{SST} \times W$$
$$r^2 = 0.391, \ n = 89, \ P < 0.001 \tag{10}$$

Obviously, the correlations are much weaker than the corresponding relationships in the open SCS in all three cases. In fact, the correlation between Chl_a and SST is not statistically significant. Even when both SST and wind speed are considered together,
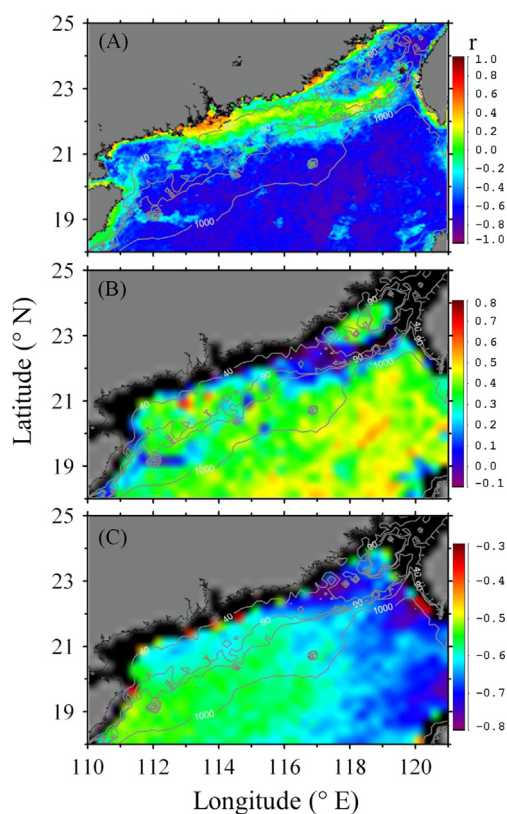
Fig. 8. The distributions of the correlation coefficients between (A) Chl_a and SST in 2002–2012, and (B) Chl_a and wind speed in 2002–2009 and (C) SST and wind speed in 2002–2009 in each pixel in the NoSoCS and adjacent open SCS. The correlation coefficients are all significant with $P < 0.05$. Those pixels with $P > 0.05$ are treated as having correlation coefficients of zero or no correlation.

the correlation coefficient is only moderate. Spatially, significant negative correlation coefficients, < -0.6, between Chl_a and SST are found only in about a third of the NoSoCS at around the southwestern end of the Taiwan Bank and at the southwestern corner of the Shelf-sea northeast of the Hainan Island. The positive correlation coefficients between Chl_a and wind speed seldom exceed 0.4 and they generally co-locate with the significant negative correlation coefficients between Chl_a and SST. On the other hand, SST remains moderately negatively correlated with wind speed, with correlation coefficients mostly between -0.5 and -0.8, over the entire NoSoCS as in the open SCS. Thus, while surface cooling and wind-induced vertical mixing also occurs in the NoSoCS as in the open SCS, they are not the only or even the primary processes that drive the seasonal variations in Chl_a in much of the Shelf-sea.

3.5. Sub-regional phenomenon – riverine input from the Pearl River

A striking feature in the distributions of the correlation coefficients between monthly average Chl_a and SST and between monthly average Chl_a and wind speed in individual pixels in the NoSoCS is a tongue of water that extends northeastward from the mouth of the Pearl River into the middle shelf with positive correlation coefficients in the former and no correlation or slightly negative correlation coefficients in the latter (Fig. 8A, B). This tongue of water co-locates approximately with the tongue of water with elevated Chl_a that represents the Pearl River plume at peak flow in July (Fig. 5).The correlation coefficient between Chl_a and SST reaches 0.5 at the mouth of the Pearl River and it decreases progressively to around 0 in the outer shelf. These patterns are consistent with the influence of the Pearl River plume

on biological production in the NoSoCS. Since the enhancement of phytoplankton growth by the Pearl River outflow reaches a maximum when the discharge of the Pearl River reaches a maximum in June and July (Figs. 5 and 6D; Guo et al., 2008; Wong et al., 2007a) when SST also reaches a maximum (Fig. 6C), in areas where the influence of the input from the Pearl River dominates, Chl_a will be positively correlated to SST. On the other hand, July is characterized by low, although not the lowest, wind speed in the NoSoCS (Fig. 6B), and this may have accounted for the poor or negative correlation between Chl_a and wind speed. In contrast, in the open SCS where the influence of the Pearl River outflow is negligible, the correlation coefficients between Chl_a and SST are invariably negative while the correlation coefficients between Chl_a and wind speed are invariably positive (Fig. 8).

The annual average Chl_a in the middle shelf is 0.53 ± 0.07 mg m^{-3} (Table 2). A concentration at twice of that value, or 1.1 mg m^{-3}, may be considered to be a significantly elevated concentration as it clearly exceeds the inter-annual variations (Table 2) and the uncertainty in the estimation of Chl_a by remote sensing (Fig. 2B). Between April and September, the areal coverage of waters with concentrations above this value in the middle and outer shelf in the patch of Chl_a-rich water that extends from the Pearl River mouth (Fig. 5) may then be used to signify the areas where the biological production has been enhanced by the Pearl River plume and to evaluate the seasonal evolution of the River plume. Furthermore, the longitude of 113.8°E, that approximately bisects the Pearl River mouth, may be used as the boundary to separate the eastward and the westward propagation of the River plume away from the River mouth. A westward propagation indicates Coriolis deflection as a dominant factor that determines the direction of propagation of the River plume as observed at many river mouths in the northern hemisphere (Mann and Lazier, 1996), while an eastward propagation indicates that Coriolis deflection has been overwhelmed by other driving forces such as the direction of the prevailing wind on the Pearl River plume (Gan et al., 2009a, 2009b, 2010). The resulting monthly areal coverage of water with elevated Chl_a in the middle and outer shelf east and west of the Pearl River mouth between April and September is estimated and the results are shown in Fig. 9. Water with such an elevated Chl_a is not found in the middle or outer shelf in the remainder of the year. The eastward aerial coverage of the water with elevated Chl_a, at around 80 km^2, is minimal in April and May. It increases abruptly to around 5000 km^2 in June and reaches a maximum of around 7000 km^2 in July before it drops off to around 2000 km^2 in August and September. Temporal changes in the area of the westward aerial coverage of the River plume are not as noticeable. The areal coverage, at around 50 km^2, is again minimal in April and May. It increases to only about 500 km^2 in June and stays relatively constantly through September. The westward aerial coverage of the plume constitutes about 40% of the total areal coverage in April
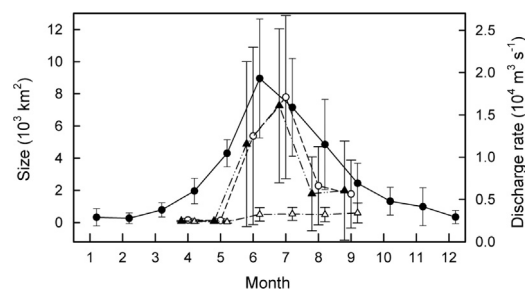
Fig. 9. The climatological monthly average Pearl River discharge (●), and, the monthly total areal coverage (○), areal coverage west (▲) and east (△) of the Pearl River mouth of the Pearl River plume in the middle and outer shelf. The error bars represent one standard deviation from the average values.

and May, $< 10\%$ in June and July, and 30% in August and September. Thus, in April and May when the river flow is low, the Pearl River plume is hardly detectable in the middle shelf as its presence is confined largely to within the inner shelf. Since the southwest monsoon has not yet arrived, the Coriolis deflection plays a major role in the propagation of the plume and leads to its significant westward aerial coverage. When the flow reaches its peak and the plume expands into the middle and outer shelf in June and July, the southwest monsoon becomes firmly established (Fig. 3). The predominance of the eastward aerial coverage of the Pearl River plume indicates that its propagation is driven primarily by wind and these patterns are consistent with the results from numerical modeling (Gan et al., 2009a, 2009b, 2010). The lower river flow and the weakening and eventual reversion of the southwest monsoonal wind to the northeast monsoonal wind in August and September (Figs. 3 and 6A) result in the reduced total areal coverage of the plume in the middle and outer shelf and the increased contribution of the westward aerial coverage. This is a distinctive feature in the propagation of the Pearl River plume that distinguishes it from many other river plumes, such as the Columbia River plume and the Chesapeake Bay plume (Mann and Lazier, 1996; Pan et al., 2008, 2010; Thomas and Weatherbee, 2006), whose propagation follows the effect of Coriolis deflection exclusively. Between October and March, high Chl_a that associates with the Pearl River outflow is confined to within the inner shelf. Its presence cannot be easily distinguished from the generally elevated Chl_a along the entire coast.

3.6. Sub-regional phenomenon – coastal upwelling

The upwelling water at the shelf edge off the Taiwan Bank may be characterized by its elevated Chl_a (Hong et al., 2009, 2011; Shang et al., 2011; Shen et al., 2008; Tang et al., 2002, 2004) and this surface expression can be clearly isolated from that of the coastal water, which has similar characteristics, between April and September (Fig. 5). The average Chl_a in the middle and outer shelf during the southwest monsoonal season are 0.55 ± 0.13 and 0.22 ± 0.14 mg m^{-3} respectively (Table 2). Thus, Chl_a > 1 mg m^{-3} would indicated a significantly elevated concentration far exceeding what may be caused by inter-annual and spatial variations. This criterion is then used for capturing the effect of the upwelling water off the Taiwan Bank (Fig. 5). The resulting areal coverage, around 4×10^3 km^2, and average Chl_a, about 1.3 mg m^{-3}, do not vary greatly from month to month (Fig. 10A, C). There is a suggestion that the areal coverage may have been slightly larger after July, the peak of the southwest monsoon. The depression in SST ranges between 0.7 and 2 °C (Fig. 10B). The maximum depression occurs in June. In the rest of the year between October and March, while upwelling may still occur (Hong et al., 2009, 2011; Hu et al., 2003, 2010; Shang et al., 2011; Shen et al., 2008; Tang et al., 2002, 2004), it cannot be characterized by remote sensing readily as the signals of higher Chl_a and lower SST are masked by the intrusion of coastal water with similar characteristics from the Taiwan Strait. The lower SST is further masked by surface cooling in the winter.

The upwelling water off the northeast coast of the Hainan Island during the southwest monsoonal season (Jing et al., 2009; Song et al., 2012; Su and Pohlmann, 2009) appears as an isolated patch of colder water in the inner and middle shelf in May through September (Fig. 4). The average SST values in the inner and middle shelf during the southwest monsoonal season in the summer are 28.0 ± 0.3 and 28.4 ± 0.3 °C, respectively (Table 2). Thus, a depression in SST of > 1 °C relative to the average SST in the inner shelf (Fig. 4) would have exceeded any inter-annual variations in and spatial variations between the inner and middle shelf and would suggest the effect of upwelling. The areal coverage of the
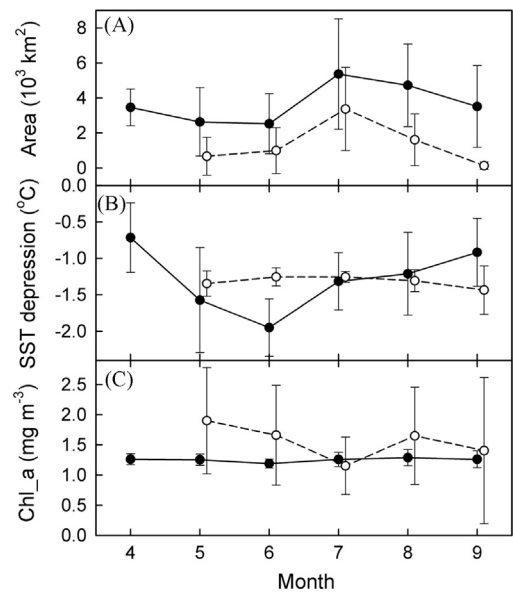

Fig. 10. The climatological monthly average (A) areal coverage, (B) depression in SST, and (C) Chl_a of the upwelling waters off the Taiwan Bank (•) and the northeastern coasts of the Hainan Island (○) between April and September. The error bars represent one standard deviation from the average values.

upwelling water ranges between 100 and 3400 km^2. It is close to the minimum in May and June and it reaches the maximum in July before it drops back to the minimum value in September (Fig. 10A). The monthly average depression in SST stays approximately constant at around 1.3 °C (Fig. 10B). Correspondingly, the monthly average Chl_a in this patch of colder water ranges between 1.1 and 1.9 mg m^{-3} (Fig. 10C). Nevertheless, whether this elevation in Chl_a may be attributed entirely to the enhancement of biological productivity by upwelling is uncertain as, unlike the suppression in SST, it is not cleanly separated from the higher Chl_a along the coast (Fig. 5).

Quantitatively characterizing the upwelling water off Dongshan during the southwest monsoonal season (Gan et al., 2009a, 2009b, 2010; Hong et al., 2009, 2011; Hu et al., 2003, 2010; Jing et al., 2009; Shang et al., 2011; Tang et al., 2002, 2004) is difficult as the elevation in Chl_a and the suppression of SST that are associated with the upwelling can be masked by the general elevation in Chl_a along the coast (Fig. 5), and the intrusion of the cold coastal water from the Taiwan Strait (Hu et al., 2010) respectively. Thus, it is not attempted here.

3.7. Sub-regional phenomenon – activities of internal waves off the shelf break

Internal waves can reach the entire outer shelf-upper slope of the NoSoCS where they undergo transformation and even destruction and these waves are the strongest in the summer when the stratification is the strongest (Guo et al., 2012; Li et al., 2008; Qu et al., 2007; Shaw et al., 2009). The average SST and Chl_a along the isobaths in July, at the height of the summer season, between 2002 and 2012 in the NoSoCS and the adjacent upper slope in the open SCS are shown in Fig. 11A. SST stays uniformly high, > 29.03 °C, while Chl_a stays uniformly low, about 0.11–0.12 mg m^{-3}, at water depths exceeding 500-m. These values are typical of the summertime conditions in the tropical/subtropical oligotrophic SCS (Liu et al., 2002, 2013; Tseng et al., 2005). However, in the shallower waters in the upper slope, SST drops abruptly by about 0.1 °C to a minimum of 28.94 °C at the 340-m isobaths before it rises again at shallower depths. Concomitantly, Chl_a increases by about 0.04 mg m^{-3} and reaches 0.17 mg m^{-3} at the 340-m isobaths. It
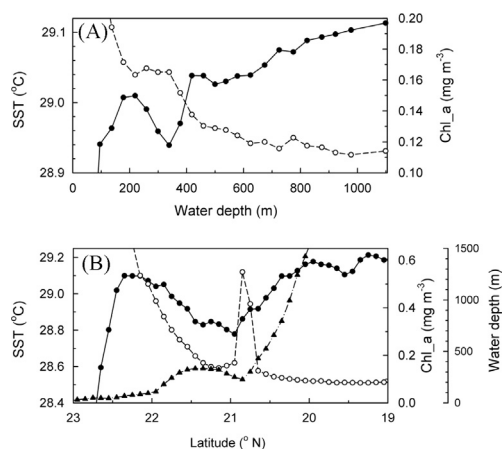
Fig. 11. (A) The average SST (●) and Chl_a (○) along isobaths in the NoSoCS and the adjacent open SCS. (B) The average SST (●), Chl_a (○) and water depth (▲) between 19 and 23°N along the longitudinal band of 116.3 to 117.3°E in July between 2002 and 2012.

then stays relatively constant until the 200-m isobaths is reached. At shallower depths in the NoSoCS, Chl_a rises to even higher concentrations. The lower SST and higher Chl_a in the upper slope are consistent with the effects of the actions of the internal waves which can bring the cooler and more nutrient-replete sub-surface water to the mixed layer along the entire outer shelf-upper slope (Guo et al., 2012; Pan et al., 2012).

The actions of the internal waves are particularly strong in the part of the Dongsha Plateau north of the Dongsha Atoll (Guo et al., 2012; Liu et al., 2006; Pan et al., 2012). The average SST and Chl_a along the longitudinal band of 116.3–117.3°E from 23° to 19°N in July between 2002 and 2012 are shown in Fig. 11B. This longitudinal band extends from the NoSoCS (north of 21.8°N), through the Dongsha Plateau (21.5–20.5°N) into the open SCS (south of 20.5°N) (Fig. 1). A minimum in SST, dipping to below 28.8 °C, is indeed found in the Dongsha Plateau. This minimum SST is about 0.2–0.3 °C lower than those found at the outer shelf-upper slope of the NoSoCS (Fig. 11A). Concomitantly, Chl_a in the Dongsha Plateau, while mostly at an elevated level of about 0.2 mg m^{-3}, which is similar to those found at the outer shelf-upper slope of the NoSoCS, can be punctuated by much higher concentrations as indicated by the concentration of 0.6 mg m^{-3} at 20.8°N. These patterns in SST and Chl_a are consistent with the area north of the Dongsha Atoll as the preferential site where some of the strongest internal waves in the world undergo transformation and dissipation and make nutrients in the subsurface water available for supporting primary production (Liu et al., 2006; Pan et al., 2012). Pan et al. (2012) reported similar findings by comparing the temperature, Chl_a and the concentrations of nutrients in the mixed layer in the areas north, east and south of the Dongsha Atoll in the path of the propagation of the internal waves and at the SEATS site in the open SCS outside of the path of propagation of the internal waves.

4. Conclusions

The seasonal variations in Chl_a and PP$_{eu}$ in the NoSoCS follow a unique pattern that is different from that in the adjacent open SCS and those generally found in the polar, temperate and tropical waters, with two distinct maxima in December/January and in July, and two minima in April/May and in September. Unlike in the open SCS, enhanced vertical mixing in the winter by surface cooling and wind-induced mixing is not the only, or even the dominant, process that controls this seasonal pattern as Chl_a is

not significantly correlated to SST and only weakly correlated to wind speed. The other processes that may contribute to this unique seasonal pattern include: (a) terrestrial input of nutrients, especially through the discharge from the Pearl River, which reaches a maximum in the summer; (b) summer coastal upwelling off Hainan Island and Dongshan, and year-round upwelling off the Taiwan Bank, and (c) the activities of internal waves at the outer shelf-upper slope.

References

Bailey, S.W., Werdell, P.J., 2006. A multi-sensor approach for the on-orbit validation of ocean color satellite data products. Remote Sens. Environ. 102, 12–23. http://dx.doi.org/10.1016/j.rse.2006.01.015.

Behrenfeld, M.J., Falkowski, P.G., 1997. Photosynthetic rates derived from satellite-based chlorophyll concentration. Limnol. Oceanogr. 42 (1), 1–20.

Cai, W.-J., 2011. Estuarine and coastal ocean carbon paradox: CO$_2$ sinks or sites of terrestrial carbon incineration? Annu. Rev. Mar. Sci. 3, 123–145.

Callahan, J., Dai, M., Chen, R.F., Li, X.L., Lu, Z.M., Huang, W., 2004. Distribution of dissolved organic matter in the Pearl River Estuary, China. Mar. Chem. 89, 211–224. http://dx.doi.org/10.1016/j.marchem.2004.02.013.

Chen, C.-T.A., 2003. New vs. export production on the continental shelf. Deep-Sea Res. II 50, 1327–1333.

Chen, Y.L., 2005. Spatial and seasonal variations of nitrate-based new production and primary production in the South China Sea. Deep-Sea Res. I 52, 319–340.

Chen, Y.L., Chen, H.-Y., 2006. Seasonal dynamics of primary and new production in the northern South China Sea: the significance of river discharge and nutrient advection. Deep-Sea Res. II 53 (6), 971–986.

Chen, Y.L., Chen, H.-Y., Karl, D.M., Takahashi, M., 2004. Nitrogen modulates phytoplankton growth in spring in the South China Sea. Cont. Shelf Res. 24, 527–541.

Chu, P.C., Lu, S., Chen, Y., 1997. Temporal and spatial variabilities of the South China Sea surface temperature anomaly. J. Geophys. Res. 102 (C9), 20937–20955.

Dai, M., Zhai, W., Cai, W., Callahan, J., Huang, B., Shang, S., Huang, T., Li, X., Lu, Z., Chen, W., Chen, Z., 2008. Effects of an estuarine plume-associated bloom on the carbonate system in the lower reaches of the Pearl River estuary and the coastal zone of the northern South China Sea. Cont. Shelf Res. 28, 1416–1423.

Dai, M., Cao, Z., Guo, X., Zhai, W., Liu, Z., Yin, Z., Xu, Y., Gan, J., Hu, J., Du, C., 2013. Why are some marginal seas sources of atmospheric CO$_2$? Geophys. Res. Lett. 40, 2154–2158. http://dx.doi.org/10.1002/grl.50390.

Dai, M., Gan, J., Han, A., Kung, H.S., Yin, Z., 2014. Physical dynamics and biogeochemistry of the Pearl River plume. In: Bianchi, T., Allison, M., Cai, W.-J. (Eds.), Biogeochemical Dynamics at Major River-Coastal Interfaces. Linkages with Global Change. Cambridge University Press, New York, pp. 321–352.

Gan, J., Li, H., Curchitser, E.N., Haidvogel, D.B., 2006. Modeling South China Sea circulation: response to seasonal forcing regimes. J. Geophys. Res. 111, C06034. http://dx.doi.org/10.1029/2005JC003298.

Gan, J., Cheung, A., Guo, X., Li, L., 2009a. Intensified upwelling over a widened shelf in the northeastern South China Sea. J. Geophys. Res. 114, C09019. http://dx.doi.org/10.1029/2007JC004660.

Gan, J., Li, L., Wang, D., Guo, X., 2009b. Interaction of a river plume with coastal upwelling in the northeastern South China Sea. Cont. Shelf Res. 29, 728–740.

Gan, J., Lu, Z., Dai, M., Cheung, A.Y.Y., Liu, H., Harrison, P., 2010. Biological response to intensified upwelling and to a river plume in the northeastern South China

Sea: a modeling study. J. Geophys. Res. 115, C09001. http://dx.doi.org/10.1029/2009JC005569.

Gordon, H.R., Morel, A., 1983. Remote Assessment of Ocean Color for Interpretation of Satellite Visible Imagery. Springer, New York.

Guo, X., Cai, W.-J., Zhai, W., Dai, M., Wang, Y., Chen, B., 2008. Seasonal variations in the inorganic carbon system in the Pearl River (Zhujiang) estuary. Cont. Shelf Res. 28, 1424–1434.

Guo, C., Vlasenko, V., Alpers, W., Stashchuk, N., Chen, X., 2012. Evidence of short internal waves trailing strong internal solitary waves in the northern South China Sea from synthetic aperture radar observations. Remote Sens. Environ. 124, 542–550.

Han, A., Dai, M., Kao, S.-J., Gan, J., Li, Q., Wang, L., Zhai, W., Wang, L., 2012. Nutrient dynamics and biological consumption in a large continental shelf system under the influence of both a river plume and coastal upwelling. Limnol. Oceanogr. 57 (2), 486–502.

Ho, T.-Y., Yang, H.-H., Pan, X., Wong, G.T.F., Shiah, F.-K., 2015. Controls on temporal and spatial variations of phytoplankton pigment distribution in the northern South China Sea. Deep-Sea Res. II, 117, 65–85. http://dx.doi.org/10.1016/j.dsr2.2015.05.015.

Hofmann, E.E., Cahill, B., Fennel, K., Friedrichs, M.A.M., Hyde, K., Lee, C., Mannino, A., Najjar, R.G., O'Reilly, J.E., Wilkin, J., Xue, J., 2011. Modeling the dynamics of continental shelf carbon. Annu. Rev. Mar. Sci. 3, 93–122. http://dx.doi.org/10.1146/annurev-marine-120709-142740.

Holman, R., Haller, M.C., 2013. Remote sensing of the nearshore. Annu. Rev. Mar. Sci. 5, 95–113. http://dx.doi.org/10.1146/annurev-marine-121211-172408.

Hong, H., Zhang, C., Shang, S., Huang, B., Li, Y., Li, X., Zhang, S., 2009. Interannual variability of summer coastal upwelling in the Taiwan Strait. Cont. Shelf Res. 29, 479–484.

Hong, H., Chai, F., Zhang, C., Huang, B., Jiang, Y., Hu, J., 2011. An overview of physical and biogeochemical processes and ecosystem dynamics in the Taiwan Strait. Cont. Shelf Res. 31, S3–S12.

Hu, J., Kawamura, H., Hong, H., Pan, W., 2003. A review of research on the upwelling in the Taiwan Strait. Bull. Mar. Sci. 75 (3), 605–628.

Hu, J., Kawamura, H., Li, C., Hong, H., Jiang, Y., 2010. Review on current and seawater volume transport through the Taiwan Strait. J. Oceanogr. 66 (5), 591–610.

Jing, Z., Qi, Y., Hua, Z., Zhang, Y., 2009. Numerical study on the summer upwelling system in the northern continental shelf of the South China Sea. Cont. Shelf Res. 29 (2), 467–478.

Laruelle, G.G., Dürr, H.H., Slomp, C.P., Borges, A.V., 2010. Evaluation of sinks and sources of CO$_2$ in the global coastal ocean using a spatially-explicit typology of estuaries and continental shelves. Geophys. Res. Lett. 37, L15607. http://dx.doi.org/10.1029/2010GL043691.

Li, X., Zhao, Z., Pichel, W.G., 2008. Internal solitary waves in the northwestern South China Sea inferred from satellite images. Geophys. Res. Lett. 35, L13605. http://dx.doi.org/10.1029/2008GL034272.

Liu, K.K., Chao, S.-Y., Shaw, P.-T., Gong, G.-C., Chen, C.-C., Tang, T.-Y., 2002. Monsoon-forced chlorophyll distribution and primary production in the South China Sea: observations and a numerical study. Deep-Sea Res. I 49, 1387–1412.

Liu, C.-T., Pinkel, R., Hsu, M.-K., Klymak, J.M., Chien, H.-W., Villanoy, C., 2006. Nonlinear internal waves from the Luzon Strait. Eos Trans. Amer. Geophys. Union 87 (42), 449–451.

Liu, K.-K., Wang, L.-W., Dai, M., Tseng, C.-M., Yang, Y., Sui, C.-H., Oey, L., Tseng, K.-Y., Huang, S.-M., 2013. Inter-annual variation of chlorophyll in the northern South China Sea observed at the SEATS Station and its asymmetric responses to climate oscillation. Biogeosciences 10, 7449–7462.

Mann, K.H., Lazier, J.R.N., 1996. Dynamics of Marine Ecosystems: Biological-Physical Interactions in the Oceans, second ed. Blackwell Science, Massachusetts.

Maritorena, S., d'Andon, O.H.F., Mangin, A., Siegel, D.A., 2010. Merged satellite ocean color data products using a bio-optical model: characteristics, benefits and issues. Remote Sens. Environ. 114, 1791–1804. http://dx.doi.org/10.1016/j.rse.2010.04.002.

McClain, C.R., 2009. A decade of satellite ocean color observations. Annu. Rev. Mar. Sci. 1, 19–42. http://dx.doi.org/10.1146/annurev.marine.010908.163650.

Morel, A., Huot, Y., Gentili, B., Werdell, P.J., Hooker, S.B., Franz, B.A., 2007. Examining the consistency of products derived from various ocean color sensors in open ocean (case 1) waters in the perspective of a multisensor approach. Remote Sens. Environ. 111, 69–88.

Nittrouer, C.A., Brunskill, G.J., Figueiredo, A.G., 1995. Importance of tropical coastal environments. Geo-Mar. Lett. 15, 121–126.

O'Reilly, J.E., Maritorena, S., Mitchell, B.G., Siegel, D.A., Carder, K.L., et al., 1998. Ocean color chlorophyll algorithms for SeaWiFS. J. Geophys. Res. 103 (C11), 24937–24953.

Pan, X., Mannino, A., Russ, M.E., Hooker, S.B., 2008. Remote sensing of the absorption coefficients and chlorophyll a concentration in the United States southern Middle Atlantic Bight from SeaWiFS and MODIS-Aqua. J. Geophys. Res. 113, C11022. http://dx.doi.org/10.1029/2008JC004852.

Pan, X., Mannino, A., Russ, M.E., Hooker, S.B., Harding, L.W., 2010. Remote sensing of phytoplankton pigment distribution in the United States northeast coast. Remote Sens. Environ. 114, 2403–2416. http://dx.doi.org/10.1016/j.rse.2010.05.015.

Pan, X., Wong, G.T.F., Shiah, F.-K., Ho, T.-Y., 2012. Enhancement of biological productivity by internal waves: observations in the summertime in the northern South China Sea. J. Oceanogr. 68, 427–437. http://dx.doi.org/10.1007/s10872-012-0107-y.

Pan, X., Wong, G.T.F., Ho, T.-Y., Shiah, F.-K., Liu, H., 2013. Remote sensing of picophytoplankton distribution in the northern South China Sea. Remote Sens. Environ. 128, 162–175. http://dx.doi.org/10.1016/j.rse.2012.10.014.

Pan, X., Wong, G.T.F., 2015. Remote sensing of the surface concentration of dissolved organic carbon (DOC) in the northern South China Sea Shelf-sea (NoSoCS) and adjacent waters. Deep-Sea Res. II 117, 131–142. http://dx.doi.org/10.1016/j.dsr2.2015.02.025.

Pauly, D., Christensen, V., 1995. Primary production required to sustain global fisheries. Nature 374, 255–257.

Qu, T., Du, Y., Gan, J., Wang, D., 2007. Mean seasonal cycle of isothermal depth in the South China Sea. J. Geophys. Res. 112, C02020. http://dx.doi.org/10.1029/2006JC003583.

Ramp, S.R., Tang, T.Y., 2011. A history of Taiwan/US oceanographic research in the South China Sea. Oceanography 24, 16–23. http://dx.doi.org/10.5670/oceanog.2011.90.

Shang, S., Dong, Q., Lee, Z., Li, Y., Xie, Y., Behrenfeld, M., 2011. MODIS observed phytoplankton dynamics in the Taiwan Strait: an absorption-based analysis. Biogeosciences 8, 841–850.

Shaw, P.T., Chao, S.Y., 1994. Surface circulation in the South China Sea. Deep-Sea Res. I 41, 1663–1683.

Shaw, P.T., Ko, D.S., Chao, S.Y., 2009. Internal solitary waves induced by flow over a ridge: with applications to the northern South China Sea. J. Geophys. Res. 114, C02019. http://dx.doi.org/10.1029/2008JC005007.

Shen, S., Leptoukh, G.G., Acker, J.G., Yu, Z., Kempler, S.J., 2008. Seasonal variations of chlorophyll a concentration in the northern South China Sea. IEEE Geosci. Remote Sens. Lett. 5 (2), 315–319.

Song, X., Lai, Z., Ji, R., Chen, C., Zhang, J., Huang, L., Yin, J., Wang, Y., Lian, S., Zhu, X., 2012. Summertime primary production in northwest South China Sea: Inter-action of coastal eddy, upwelling and biological processes. Cont. Shelf Res. 48, 110–121.

Strickland, J.D.H., Parsons, T.R., 1972. A Practical Handbook of Sea-Water Analysis, 2nd ed. Fishery Research Board, Ottawa.

Su, J., Pohlmann, T., 2009. Wind and topography influence on an upwelling system at the eastern Hainan coast. J. Geophys. Res. 114, C06017.

Szeto, M., Werdell, P.J., Moore, T.S., Campbell, J.W., 2011. Are the world's oceans optically different? J. Geophys. Res. 116, C00H04. http://dx.doi.org/10.1029/2011JC007230.

Tang, D., Kester, D.R., Ni, I.-H., Kawamura, H., Hong, H., 2002. Upwelling in the Taiwan Strait during the summer monsoon detected by satellite and shipboard measurements. Remote Sens. Environ. 83, 457–471.

Tang, D., Kawamura, H., Guan, L., 2004. Long-time observation of annual variation of Taiwan Strait upwelling in summer season. Adv. Space Res. 33, 307–312.

Tang, S., Chen, C., Zhan, H., Zhang, J., Yang, J., 2008. An appraisal of surface chlorophyll estimation by satellite remote sensing in the South China Sea. Int. J. Remote Sens. 29 (21), 6217–6226.

Thomas, A.C., Weatherbee, R.A., 2006. Satellite-measured temporal variability of the Columbia River plume. Remote Sens. Environ. 100, 167–178.

Tseng, C.-M., Wong, G.T.F., Lin, I.-I., Wu, C.-R., Liu, K.-K., 2005. A unique seasonal pattern in phytoplankton biomass in low-latitude waters in the South China Sea. Geophys. Res. Lett. 32, L08608. http://dx.doi.org/10.1029/2004GL022111.

Wang, D., Zhuang, W., Xie, S.-P., Hu, J., Shu, Y., Wu, R., 2012. Coastal upwelling in summer 2000 in the northeastern South China Sea. J. Geophys. Res. 117, C04009. http://dx.doi.org/10.1029/2011JC007465.

Wong, G.T.F., Ku, T.-L., Mulholland, M., Tseng, C.-M., Wang, D.-P., 2007a. The SouthEast Asian Time-series Study (SEATS) and the biogeochemistry of the South China Sea – an overview. Deep-Sea Res. II 54, 1434–1447. http://dx.doi.org/10.1016/j.dsr2.2007.05.012.

Wong, G.T.F., Tseng, C.-M., Wen, L.-S., Chung, S.-W., 2007b. Nutrient dynamics and N-anomaly at the SEATS station. Deep-Sea Res. II 54, 1528–1545. http://dx.doi.org/10.1016/j.dsr2.2007.05.011.

Upwelling ecosystem in the Southern Taiwan Strait. Cont. Shelf Res. 31, S1–S76.

Wong, G.T.F., Pan, X., Li, K.-Y., Shiah, F.-K., Ho, T.-Y., Guo, X., 2015. Hydrography and nutrient dynamics in the Northern South China Sea Shelf-sea (NoSoCS). Deep-Sea Res. II 117, 23–40. http://dx.doi.org/10.1016/j.dsr2.2015.02.023.

Yin, K., 2002. Monsoonal influence on seasonal variations in nutrients and phytoplankton biomass in coastal waters of Hong Kong in the vicinity of the Pearl River estuary. Mar. Ecol. Prog. Ser. 245, 111–122.

Yoder, J.A., McClain, C.R., Feldman, G.C., Esaia, W.E., 1993. Annual cycles of phytoplankton chlorophyll concentrations in the global ocean: a satellite view. Glob. Biogeochem. Cycles 7 (1), 181–193.

Yoder, J.A., Schollaert, S.E., O'Reilly, J.E., 2002. Climatological phytoplankton chlorophyll and sea surface temperature patterns in continental shelf and slope waters off the northeast U.S. coast. Limnol. Oceanogr. 47 (3), 672–682.

Zhang, C., Hu, C., Shang, S., Muller-Karger, F.E., Li, Y., Dai, M., Huang, B., Ning, X., Hong, H., 2006. Bridging between SeaWiFS and MODIS for continuity of clorophyll-a concentration assessments off Southeastern China. Remote Sens. Environ. 102, 250–263.